ASME Journal of Turbomachinery
Online journal at:
https://asmedigitalcollection.asme.org/turbomachinery

A New Perspective on Internal Turbine Blade Cooling by Perforated Blockages and Pin-Fins

S. W. Schekman[1]
School of Mechanical, Industrial and Aeronautical Engineering,
University of the Witwatersrand,
Johannesburg 2000, South Africa
e-mail: sjouke.schekman@wits.ac.za

T. Kim
School of Mechanical, Industrial and Aeronautical Engineering,
University of the Witwatersrand,
Johannesburg 2000, South Africa;
College of Aerospace Engineering,
Nanjing University of Aeronautics and Astronautics,
Nanjing 210016, China
e-mail: tong.kim@wits.ac.za

The cooling configuration, sequentially combining perforated blockages (forming blockage jets) and a pin-fin array inside the trailing-edge of a turbine blade has been perceived unsuitable due to the presumed inferior thermal performance ($\eta < 1.0$). In the present study, we provide a new perspective on this particular cooling configuration, based on fluidic mechanisms, newly established in a better representative setup for blockage jets aligned with pin-fins, accounting for relevant heat transfer surfaces. To this end, heat transfer on the blockage, pin-fin, and end-wall surfaces was measured at a selected Reynolds number of $Re_D = 26{,}000$ using a thermochromic liquid crystal technique. Flow field mapping by particle image velocimetry and oil–dye flow visualization were supplementally performed. We demonstrate, contrary to previous studies that the thermal performance of the blockage pin-fin configuration can be e.g., $\eta = 1.1$ if the blockages and pin-fins are arranged to maximize both elements' thermofluidic advantages. Our data further suggest that unlike conventional pin-fin configurations subjected to uniform coolant stream, the blockage pin-fin configuration can offer a better performance with fewer pin-fin rows used.

[DOI: 10.1115/1.4065616]

Keywords: heat transfer, internal cooling, perforated blockages, pin-fins, trailing-edge, thermal performance, fluid dynamics and heat transfer phenomena in compressor and turbine components of gas turbine engines

1 Introduction

A gas turbine operates more efficiently at higher combustion temperatures with the first row of stators (or airfoils) being exposed to excessive temperatures of 1850 K [1]. It, therefore, necessitates proper cooling of such airfoils, which is achieved by redirecting some airflow as coolant from the compressor stages. However, the introduction of cooling compromises the overall engine efficiency at the expense of an analogous pumping power. The cooling performance of a given cooling configuration can thus be assessed by a product of the increased heat transfer offered against the increased unit pumping power, the thermal performance [2,3], given as:

$$\eta = \frac{\mathrm{Nu}/\mathrm{Nu}_0}{(f/f_0)^{1/3}} \tag{1}$$

where Nu is the Nusselt number and f is the friction factor with each normalized against the respective values for a smooth or empty channel denoted by the subscript of 0.

The cooling of a turbine blade at the trailing-edge can be especially difficult given the aerodynamic and manufacturing constraints associated with the requirement for a thin trailing-edge (Fig. 1(*a*)). Its internal cooling can be implemented by, among other techniques, pin-fin arrays (Fig. 1(*b*)) and perforated blockage plates (Fig. 1(*c*)). A combination of the two techniques is referred to, here, as a "blockage pin-fin" (BPF) configuration as shown in Fig. 1(*d*). The total heat transfer in the BPF configuration is made up of the heat transfer from end-wall surfaces, pin-fin surfaces, and the surfaces of perforated blockages.

For a pin-fin (PF) configuration (Fig. 1(*b*)), the relationship between pin-fins and end-wall heat transfer has been previously established. VanFossen [4] determined that for $\mathrm{Re}_D \leq 60{,}000$, a pin-fin aspect ratio of $H/D < 2.0$, the average heat transfer at the pin-fins was approximately 35% higher than at end-wall surfaces. Goldstein et al. [5] and Lawson et al. [3] reported similar results to the forgoing case for $H/D = 2.0$ and 1.0, each considering $\mathrm{Re}_D \leq 30{,}000$. There exists a tendency for higher Reynolds numbers to result in a decrease in the difference between pin-fin and end-wall surface heat transfer. This relation between end-wall and pin-fin heat transfer cannot be assumed equivalent for a BPF configuration due to a difference in end-wall flow topologies between the two cases.

Specifically, in a conventional pin-fin array that is subjected to a uniform coolant stream, a horseshoe vortex is formed around the base of each pin-fin as shown in Fig. 2(*a*) [6]. The formation of such horseshoe vortex results from the boundary layer separating from the end-wall and subsequent rolling up due to the adverse

---

[1] Corresponding author.

Manuscript received May 17, 2023; final manuscript received May 20, 2024; published online June 17, 2024. Assoc. Editor: Xueying Li.

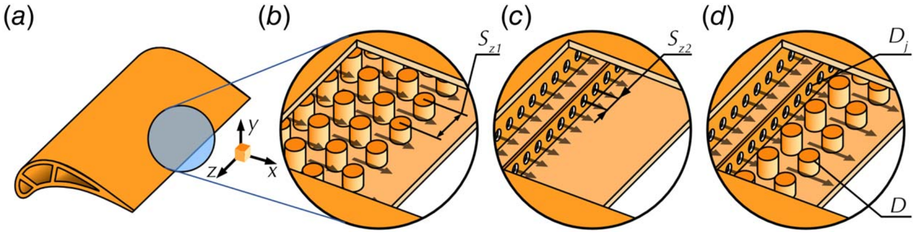

Fig. 1 Turbine blade internal cooling configurations at the trailing-edge: (*a*) a CAD design of a high pressure (HP) gas turbine blade, (*b*) a pin-fin array, (*c*) perforated blockage plates, and (*d*) a combination of perforated blockage and pin-fin array

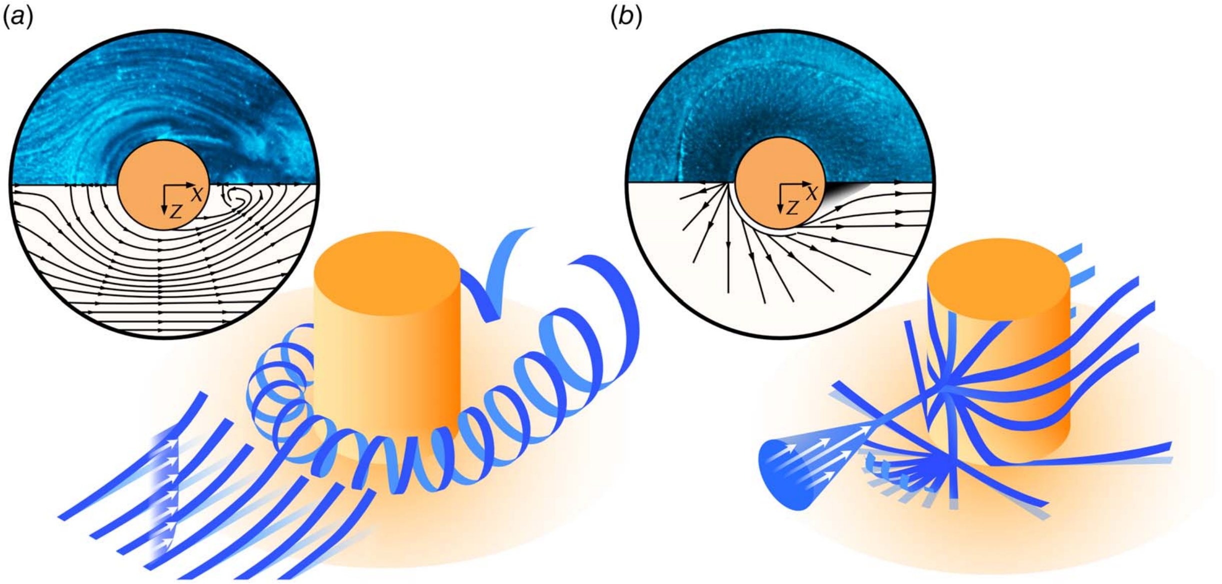

Fig. 2 Flow schematic and end-wall topology distinction between flow structure around a circular pin-fin subjected to (*a*) a uniform type of flow [6] and (*b*) a jet type of flow [7]

pressure gradient set by the downstream pin-fins. In a BPF configuration, however, there is no end-wall flow upstream of the pin-fins due to the presence of the upstream blockages. The only flow interacting with the pin-fins is jets formed from the perforations in the blockages (here on termed as "blockage jets"). This results in a wholly unique flow field illustrated in Fig. 2(*b*) as established by Schekman et al. [7]. The flow on the end-wall surface radiates outwards from the pin-fin's leading surface itself. The uniqueness of this flow topology was not identified in previous studies of the BPF configurations.

Similar to the case for a conventional pin-fin array, the end-wall heat transfer for a perforated blockage (PB) configuration (Fig. 1(*c*)) is also established. Moon and Lau considered the end-wall heat transfer between a series of perforated blockages at $\mathrm{Re}_{Dh} =$ 10,000 and 30,000 for the perforation's center-to-center distance fixed at $S_{z2}/D_j = 2.0$. They showed that the perforated blockages increased the end-wall heat transfer by 5.0–8.0 times. A large increase in pressure drop attributed to the perforated blockages, resulting in the thermal performance of a typical PB configuration being approximately $\eta \approx 0.70$ [2,26]. Considering the significantly enlarged surface area of the blockages exposed to the coolant stream, a notable amount of heat transfer is expected to occur on the blockage surfaces as noted by Lau et al. [8]. However, no subsequent studies, to the best of the authors' knowledge, have directly measured the heat transfer on the surfaces of the perforated blockages for either perforated blockage cooling (Fig. 1(*c*)) or blockage pin-fin cooling (Fig. 1(*d*)).

A further consideration in the BPF configuration is the dependence between perforation spacing (S_{z2}/D_j) and pin-fin spacing (S_{z1}/D) as indicated in Fig. 1. These spacings determine how well aligned the blockage jets are with the pin-fins (i.e., for $S_{z2}/D = S_{z1}/D$). Prior studies of the perforated blockage cooling use a perforation spacing in the range of $1.33 \leq S_{z2}/D_j \leq 3.33$ [2,8–10]. Other spanwise spacings used for the pin-fins arrays were $2.0 \leq S_{z1}/D \leq 8.0$ by Metzger et al. [11], Goldstein and Chen [5], and Lyall et al. [12]. Lower spanwise spacing values typically resulted in higher heat transfer but a higher pressure drop through the array [12]. Following these conventions, Kan et al. [13] used the spacings of $2.14 \leq S_{z2}/D_j \leq 3.85$ and $S_{z1}/D = 2.0$. However, none of the spacings used resulted in an alignment between the perforations and the pin-fins. As such, some or all blockage jets would not directly impinge on the pin-fins, and each pin-fin in the first row was subjected to a unique flow field. Those pin-fins that were subjected to blockage jet impingement more directly on their surface, exhibited significantly higher local heat transfer on the end-wall (2.0–4.0 times higher). The mismatch between perforation spacing and pin-fin spacing is considered to further misrepresent the thermal performance of the BPF cooling configuration.

A BPF configuration has thus been perceived to provide an inferior thermal performance, $\eta < 1.0$ (i.e., lower than that of an empty channel), specifically $\eta \approx 0.8$ by Kan et al. [13] or even $\eta \approx 0.2$ by Kim et al. [14]. A PF configuration, in sharp contrast, can have a superior thermal performance of $\eta \approx 3.0$ by Lawson et al. [3]. Due to the presumed inferior performance, the BPF configuration has not received significant attention. Over and above the mismatch between perforation spacing and pin-fin spacing, Kim et al. [14] only measured the end-wall heat transfer, and Kan et al. [13] only measured the heat transfer on the end-wall and pin-fin surfaces. The pressure drop was measured across the entire configuration, however, considering all features of the BPF configuration (end-wall, blockages, and pin-fins).

This inferior thermal performance of the BPF configuration seems to be inaccurate or at least misrepresented. The heat transfer of all surfaces was not considered or was considered inaccurately, and non-optimal setups were utilized. Therefore, this study aims to squarely address this issue by investigating a complete thermal performance of a setup using perforations aligned with the pin-fins. To this end, heat transfer measurements in two perforated blockages and five rows of circular pin-fins have been conducted using a thermochromic liquid crystal technique. Supplementary flow measurements were conducted using particle image velocimetry and end-wall oil–dye flow visualization.

2 Experiment Details

2.1 Test Facility. The schematic representing the present test setup is illustrated in Fig. 3. An axial fan supplies ambient air into a rectangular channel with cross-sectional dimensions of $W = 200$ mm and $H = 20$ mm. Two perforated blockage plates were staggered and installed in the channel. Two blockages were used as this is considered more optimal for a BPF configuration for cooling purposes—the increase in friction factor from an additional blockage is largely negligible [2] while the end-wall heat transfer between the blockages is higher than around a pin-fin array [2,5,13], providing more benefit obtained from the additional blockage. All perforations had the same diameter of $D_j = 10$ mm. The blockage plate thickness (t) was half that of the perforation diameter ($t/D_j = 0.5$), which assumes an orifice-type jet flow [15,16].

Five rows of staggered circular pin-fins were positioned downstream of the two staggered perforated blockage plates and had a diameter (D) twice that of the perforation diameter ($D/D_j = 2.0$). The pin-fin spacings were $S_{z1}/D = 2.0$ and $S_x/D = 1.5$. To ensure the alignment of the second blockage plate perforations with the pin-fins, the perforation spacing was set as $S_{z2}/D_j = 2.0$ ($S_{z2}/D = 1.0$). These variables were predicted based on prior testing to result in a more optimal BPF configuration compared to that of the comparison case by Kan et al. [13]. Both the perforation diameter and thickness (D_j and t) may prove difficult to achieve in practice due to the small scales. They are considered, regardless, as a representation of a theoretical and optimal BPF configuration.

The pin-fins had an aspect ratio $H/D = 1.0$. This was based on previous studies using pin-fin arrays [3,11,12]. Both blockages had 10 perforations. For the second blockage, the first and tenth perforations were split into two half circles at the channel edge. This was primarily to maintain a constant reduction in flow area across both blockages ($A_{perforation} = 0.196A_{channel}$).

The first pin-fin row was positioned $x/D = 1.0$ downstream from the exit of the second blockage. The distance between the perforated blockage plates, relative to the height of the channel was $l_B/H = l_B/D = 1.5$. The pin-fins, perforated blockages, and bottom end-wall were machined from aluminum for heat transfer measurements. The channel sidewalls and lid (top end-wall) were machined from transparent Perspex to allow for optical access using thermal and velocity field mapping techniques (to be discussed later). A sidewall was machined for static pressure taps, which were positioned along the channel at selected locations as indicated in Fig. 3. The furthest downstream location was positioned $x/D = 10$ from the second perforation blockage. The Reynolds number was fixed at $\mathrm{Re}_D = 26{,}000$, based on the pin-fin diameter (or $\mathrm{Re}_{Dh} = 10{,}000$ based on the hydraulic diameter of the test rectangular channel). Fully turbulent flow would thus be expected for the blockage jets [17]. This Reynolds number falls in the range that is accepted to cover most turbine applications of $3.0 \times 10^3 < \mathrm{Re}_D < 5.0 \times 10^4$ [11].

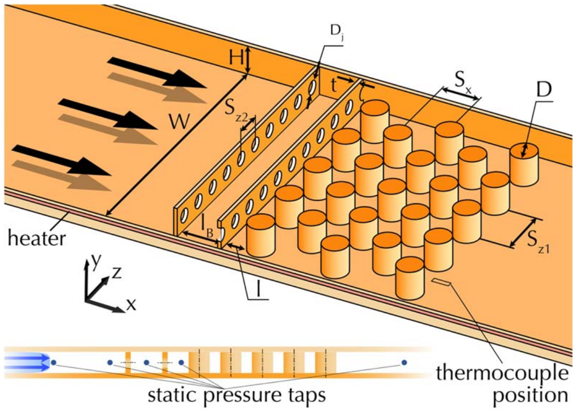

Fig. 3 Cutaway of test setup schematic showing two perforated blockage plates and five staggered rows of short circular pin-fins with left sidewall and upper end-wall removed

2.2 Flow Field Mapping Using Particle Image Velocimetry. The impingement of blockage jets on a pin-fin array was mapped by particle image velocimetry (PIV) as shown in Fig. 4(*a*). Clear glass pin-fins were implemented to further increase laser penetration and increase flow illumination between the pin-fins for the mid-height plane measurements. This technique allowed for the regions that would typically be shadowed by the pin-fins, to be illuminated. The channel could be rotated 90 deg from that shown in Fig. 4(*b*) for measurement in the *x*-*y* plane.

The side walls and lid of the test setup were constructed from transparent Perspex to allow for laser illumination and imaging. Other surfaces were painted matt black to minimize reflections and light scatter. The flow field was seeded with an atomized mineral oil (Shell Ondina 901L0996) having a mean particle diameter of approximately 1 μm. The particles were introduced into the test channel upstream of the blockage plates. The position where the particles were introduced, and pressure of the seeding generator was adjusted to ensure a uniform seeding distribution in the measurement window.

The flow field was illuminated by a pulsed laser light, generated from a frequency-doubled, dual cavity Nd:YAG laser (New Wave Research™, USA), with a light wavelength of 532 nm. The measurement period is defined by two sequential pulses of the laser light sheet that are separated by a finite time interval (approximately 18 μs based on the flow measurements made using a Pitot tube).

The recorded flow field is represented by the random pattern of particle images that are mapped onto the image plane of the charge-coupled device (CCD) sensor. The camera was positioned so the optical axis was perpendicular to and focused on the laser light sheet. The images were recorded on the sensor frame that had a 2048×2048-pixel resolution and a pixel pitch of 7.4 μm. The field of view that was set up within the light sheet had a PIV measurement area of the full channel width (200 mm × 200 mm), and the image magnification factor was $M_0 \approx 0.1026$. The PIV images were divided into sub-regions referred to as interrogation areas that were 16×16 pixels in size and overlapped by 50%; hence, each velocity map contains 255×255 vectors, and the resulting vector spacing was 0.4 mm. The evaluation of the image field between two successive frames yielded an instantaneous vector map which was achieved with a Dantec Dynamic Studio V1.45 software. The ensemble-averaged velocity field for a specific location in the flow field was then evaluated over an ensemble of 124 instantaneous vector maps sampled at a frequency of 5 Hz. The measurement techniques and setup were based on the work established by Atkins and Kim [18].

2.3 End-Wall Surface Flow Visualization Using an Oil–Dye Mixture Technique. End-wall surface flow pattern was visualized

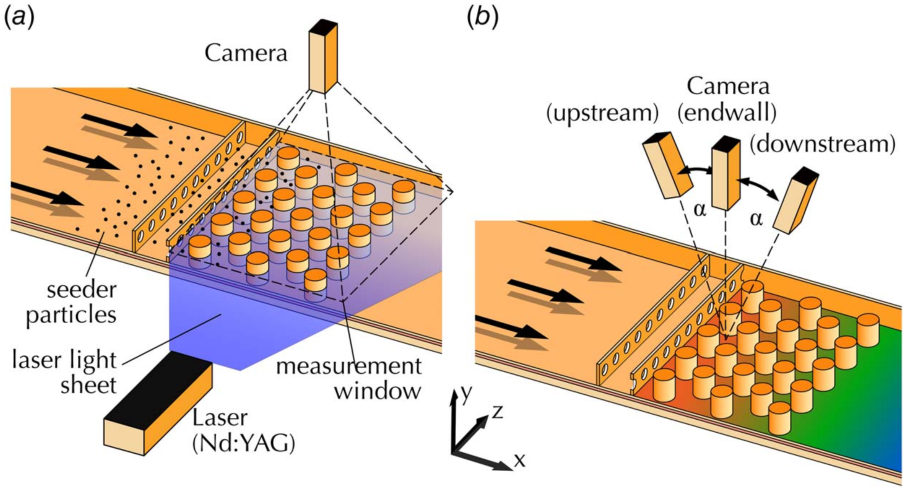

Fig. 4 Test schematics: (*a*) The particle image velocimetry (PIV) setup in the mid-height plane illumination and (*b*) The thermochromic liquid crystal (TLC) setup with $\alpha = 30$ deg

using an oil–dye mixture technique. Florescent powder was mixed with light diesel fuel, and the mixture was then applied to the end-wall surface. The aerodynamic shear stresses, at the end-wall, redistributed the mixture, and visualization of the surface flow patterns was realized. This pattern represented a time-averaged visualization of the end-wall flow topologies. Validation and interpretation of such topologies have been independently validated against near-end-wall PIV measurements in a previous study [7].

Before the application of the mixture, the surface was painted black to enhance the reflectivity. An ultraviolet (UV) light illuminated the surface flow pattern while it was being photographed. Further, the experiment was run for a sufficient length of time to allow for at least a partial evaporation of the diesel. This allowed for the patterns to be imaged with the wind tunnel turned off without the disturbed diesel mixture flowing back over the patterns, disrupting the image. More details associated with this flow visualization technique can be found in the study by Kim et al. [19].

2.4 Surface Heat Transfer Mapping Using Thermochromic Liquid Crystal.

A film heater was positioned under the end-wall surface (Fig. 3). A Teflon board was mounted beneath the heater for insulation. The heat flux (q'') used to calculate heat transfer coefficient (h) is estimated as:

$$q'' = Q_{net}/A \tag{2}$$

where A is the heating area and Q_{net} is the net heat removed by the convective flow in the channel after taking account of heat loss (i.e., $Q_{net} = Q_{input} – Q_{loss}$). Here, Q_{input} is the input power calculated from the measured input current and voltage to the film heater and Q_{loss} is the heat loss at the test Reynolds number which was conservatively calculated to be 5% of Q_{input} considering the thermal conductivity of the surrounding materials, ambient air temperature, and the end-wall temperature.

The local surface temperature was measured using thermochromic liquid crystal (TLC) painted onto the setup surfaces (end-wall, pin-fins, and perforated blockages). A 12-MP digital camera was used to capture the images. A single-point flash was used for illumination. For overhead measurements of the end-wall surfaces, the camera was placed directly overhead of the surfaces. For measurements on the vertical surfaces (perforated blockages and pin-fins), the camera was inclined by 30-deg either side of the vertical to capture the upstream and downstream sides of the surfaces (Fig. 4(*b*). To avoid parallax issues from the pin-fins obscuring end-wall measurements, a series of images were captured after repositioning the camera in both spanwise (z) and streamwise directions (x). These images were then combined in post-processing. The test rig was allowed to reach steady-state heat transfer before measurements were taken.

Calibration of the w was achieved by mounting a thin film thermocouple (Omega CO_2-K) to the end-wall surface. For the overhead images, the camera was positioned directly overhead the thermocouple. For the inclined images, the camera was positioned at 60 deg to the horizontal (accounting for the 90-deg difference in vertical and horizontal surfaces). The hue values at the thermocouple were then matched with those from the thermocouple as shown in Fig. 5. As evident there can exist a large difference between measurements at 90 deg and 60 deg. When capturing the end-wall surface, the measurement window was limited to 50% of the channel span. This limited the angle of the incoming light and reduced the variation from the outer edges of the measurement to just less than 1 °C. Regions were then combined together in post-processing to create a complete end-wall map. This had the added benefit of allowing regions of the end-wall obscured by the pin-fins to be visualized.

During testing, a large heat transfer range was noted. Specifically, the perforated blockages and pin-fin surfaces have a higher heat transfer compared to the overall end-wall surface. To account for this, the input power Q_{in} was adjusted depending on whether the vertical surfaces or end-wall was measured. This was preferred over the use of TLC with a larger temperature band to ensure greater temperature sensitivity over a given surface. Images captured during testing were then cropped and the hue values extracted. These were converted to surface temperatures using the calibration data from Fig. 5. From these values, the heat transfer coefficient (h)

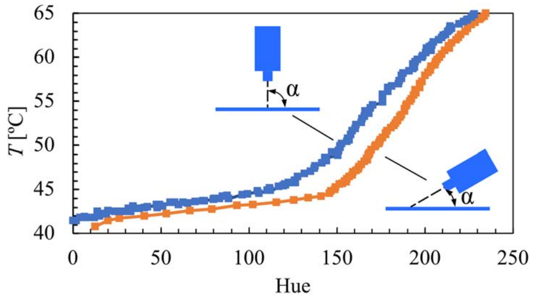

Fig. 5 Calibration curves for the present thermochromic liquid crystal (TLC) for $\alpha = 90 -$ deg and $\alpha = 30 -$ deg inclined viewpoints

was calculated as:

$$h = q''/(T_S - T_{bulk}) \tag{3}$$

where T_s was the measured surface temperature and T_{bulk} was the bulk air temperature based on $T_{bulk} = T_{in} + Q_{net}/\dot{m}C_p(x/l_{heater})$. Here, T_{in} was the measured air temperature at the channel inlet using a K-type moving air probe, $\dot{m}$ was the mass flowrate, C_p the specific heat, and x/l_{heater} was the relative distance along the length of the heater. T_{bulk} was approximately 10 K higher than T_{in} by the end of the heater. The resultant Nusselt number relative to the hydraulic diameter was:

$$\mathrm{Nu}_{Dh} = hD_h/k_f \tag{4}$$

where k_f is the thermal conductivity of air in W/m/K.

2.5 Data Reduction Parameters and Measurement Uncertainties. The Reynolds number, based on pin-fin diameter, is defined as:

$$\mathrm{Re}_D = \rho\, v_c D/\mu \tag{5}$$

where ρ is the air density in kg/m^3, μ is the air viscosity in kg/(ms), v_c is the centerline (maximum) velocity of blockage jets at exit in m/s and D is the pin-fin diameter in m. A Reynolds number, based on hydraulic diameter ($\mathrm{Re}_{\mathrm{Dh}}$), instead uses v_{avg}, the average velocity through the channel in m/s, and D_h is the hydraulic diameter in m. Velocity measurements were initially made through Pitot tube measurements and then confirmed with PIV measurements. The empty channel Nusselt number was based on [20]:

$$\mathrm{Nu}_0 = 0.022\mathrm{Re}_{Dh}^{0.8}Pr^{0.5} \tag{6}$$

where Pr is the Prandtl number. The friction factor was based on:

$$f = -\left(\frac{\Delta p}{\Delta x}\right)D_h/0.5\rho v_{avg}^2 \tag{7}$$

where p is the static pressure measured at set intervals along the length of the channel. The baseline friction factor was based on [21]:

$$f_0 = 0.507\mathrm{Re}_{D_h}^{-0.3} \tag{8}$$

Measurement uncertainties were estimated using a method as follows. If $y = f\,(x_1, x_2, \ldots, x_n)$, then the uncertainty propagated by x_i in the variable y is given by [22]:

$$\Delta y = \sqrt{\left(\frac{\delta y}{\delta x_1}\Delta x_1\right)^2 + \left(\frac{\delta y}{\delta x_2}\Delta x_2\right)^2 + \ldots + \left(\frac{\delta y}{\delta x_n}\Delta x_n\right)^2} \tag{9}$$

Using this method, the uncertainty associated with the Reynolds number was calculated to be within 1.8%. The uncertainty in the Nusselt numbers was calculated to be 4.1%. This value is lower than that typically purported for TLC measurements, but this was attributed to the measurements being conducted at a steady-state rather than using a transient approach. The uncertainty in the temperature measurement from TLC was 3.0%. The uncertainty of the instantaneous PIV velocity measurements is primarily related to the estimation of the average particle displacement within an interrogation area. The uncertainty regarding the timing of the light sheet pulses and particle lag are not considered significant sources of error. The determination of measurement uncertainty relating to particle displacement has been quantified analytically and by the generation of synthetic images with known parameter values [23–25]. To provide a reasonable estimate of measurement error, the PIV algorithm given by Westerweel [25] was applied. The displacement measurement error based on the mean particle image diameter of 2–3 pixels is 0.05 pixels. Therefore, the full-scale relative measurement error is 0.6%.

3 Discussion of Results

3.1 Mid-Height Velocity and End-Wall Heat Transfer Fields. Considering the blockage pin-fin (BPF) configuration, the mainstream in the rectangular channel is forced to pass through the perforations of the first blockage, forming blockage jets at $\mathrm{Re}_D = 26{,}000$ ($\mathrm{Re}_{Dh} = 10{,}000$) as depicted in Fig. 6(*a*). At this Reynolds number, fully turbulent blockage jets are expected. These blockage jets then impinge on the second perforated blockage. The stagnated flows are subsequently redirected away from the stagnation point and toward the upper and lower end-walls. These redirected jets and resulting end-wall flows are, however, not distinguishable in the end-wall heat transfer contours (Fig. 6(*b*)). The end-wall flows have only been discerned in the end-wall heat transfer if the blockage jets exit closer to the end-wall surfaces [2,8] and if there is a larger spanwise spacing (S_{z2}/D_j) between jets [27].

The flow is further forced through the perforations of the second blockage, forming blockage jets. These blockages jets can be broken into two groups: "even blockage jets" (via $z/D = 0.0$, ±2.0, and ±4.0) that impinge on the first row of pin-fins and

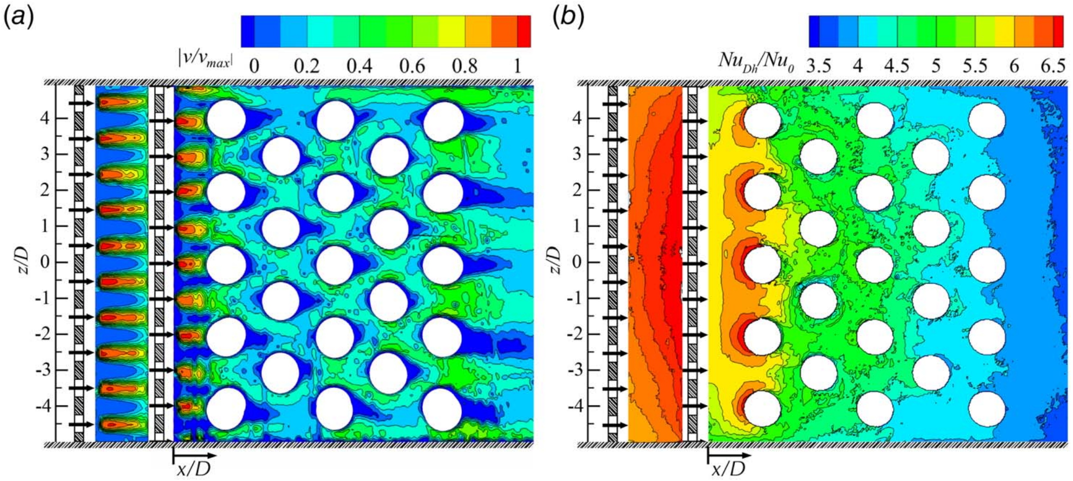

Fig. 6 Velocity field and heat transfer for the BPF configuration at $\mathrm{Re}_D = 26{,}000$: (*a*) flow fields in the mid-height plane measured with PIV where $v_{\max}$ is the centerline velocity of blockage jets at exit and (*b*) end-wall surface heat transfer measured by TLC

"odd blockage jets" (via $z/D = \pm 1.0$ and ± 3.0) that pass between the pin-fins of the first row to impinge on the second row of pin-fins as exhibited in Fig. 6(*a*). The even blockage jets have insufficient space to diffuse before impinging on the pin-fin. As such the entirety of the even blockage jets stagnate on the pin-fin surfaces and are subsequently redirected both circumferentially around the pin-fins as well as towards the end-walls as wall jet type flows. Those flows moving around the pin-fin surface then detach from the pin-fins resulting in wakes downstream of the pin-fins. The flows towards the end-wall surfaces go on to form end-wall flow structures as shown in Fig. 2(*b*). On the other hand, the odd blockage jets continue to diffuse past the first row of pin-fins with the centerline velocities decreasing accordingly. The flow directly interacting with the pin-fins in the second row is distinctly slower compared to the pin-fins of the first row as per Figs. 6(*a*) and 7. Further, the velocity contours around the second row of pin-fins are similar to those around the fourth row of pin-fins in the mid-height plane (Fig. 6(*a*)). After the first row of pin-fins, jet structures in the mid-height plane are indiscernible.

As a result of the impingement of blockage jets on the array of pin-fins, local heat transfer on TLC-painted end-wall surfaces is distributed as shown in Fig. 6(*b*). The end-wall is broken up into two specific regions: between the perforated blockages and around the pin-fin array. A very high-end-wall heat transfer occurs between the perforated blockages. Contour bands between the two perforated blockages show that end-wall heat transfer increases in magnitude in the downstream direction. Similar contours are noted in previous perforated blockage studies [2]). A larger variation of heat transfer exists around the pin-fin array than between the blockages. At the first row of pin-fins, clear semi-circular contour bands surrounding the leading-edge of the pin-fins in the first row are observed. Similar contours were noted by Kan et al. [13]. Downstream from the second row of pin-fins, there are no such contour bands, and the end-wall heat transfer decreases consistently through each row of pin-fins. Further, as convecting downstream along the pin-fin array, low-end-wall heat transfer between the outer pin-fins and channel sidewalls occurs.

To highlight local end-wall heat transfer features, the data were extracted from Fig. 6 at two transverse locations e.g., $z/D = 0.0$ and 1.0 as plotted in Fig. 7. The even blockage jet discharging at $z/D = 0.0$ exits the blockage and impinges on the first row of the pin-fin (Fig. 7(*a*)). Local end-wall heat transfer increases leading up to the first row of pin-fins and then decreases with successive rows. The centreline velocity of the even blockage jet (at $z/D = 0.0$) steeply increases after exit, peaking at $x/D = 0.5$ (i.e., $x/D_j = 1.0$ from the exit of the perforation or $x/D_j = 1.5$ from the inlet of the perforation, since $D_j/D = 0.5$). This peaking location is roughly coincident with the longitudinal location of Vena Contracta of jet flow through an orifice. After which, the centerline velocity drops to zero due to stagnation on the leading-edge of the first-row pin-fin. The odd blockage jet, discharging at $z/D = 1.0$, bypasses the first row before impinging on the second row of the pin-fins (Fig. 7(*b*)). After the first row, the centreline velocity continues to decrease. This velocity decrease is slightly more than a case without downstream pin-fins as seen in Fig. 7(*b*), indicating that the circumferential flow around the first row of pin-fins has some effect on the odd blockage jet. Due to the lower relative centreline velocity, there is a weaker flow interacting with the pin-fin, and correspondingly, lower heat transfer occurs around the second row of pin-fins compared to the first.

Initially, blockage jets impinge on the mid-span of the pin-fins. At the first pin-fin row, the only end-wall flow surrounding those pin-fins is solely from the (even) jet flows in the mid-height plane (Fig. 8(*a*)) where the jet flow does not contact the end-wall upstream of the pin-fin. The end-wall flow around the pin-fins thus is expected to resemble the flow topology in Fig. 2(*b*). This end-wall flow results in the high heat transfer around the first row of pin-fins. If sufficiently downstream, however, the blockage jets both decelerate and diffuse, contacting the end-wall surface and horseshoe vortex-like flows (like those in Fig. 2(*a*)) begin to form (Schekman et al., 2019). These features are responsible for the small local increase in end-wall heat transfer immediately upstream of the second and fourth pin-fin in Fig. 7(*b*) and the third pin-fin in Fig. 7(*a*). The variation in end-wall heat transfer in Figs. 6(*b*) and 7 is then due to a variation not only in the strength of the end-wall flows but also in the type of flow topologies. This combined variation then results in an almost monotonic decrease in the end-wall heat transfer with successive pin-fin rows, as seen in Fig. 7(*a*).

We consider next the end-wall heat transfer averaged in the transverse direction (Fig. 9). Between the blockages, the heat transfer is almost uniform with a variation of approximately $\Delta\mathrm{Nu}/\mathrm{Nu}_0 = 0.5$ across the end-wall surface and an average heat transfer of $\overline{\mathrm{Nu}_{Dh}}/\mathrm{Nu}_0 = 6.4$. This is attributed to the relatively short distance between the perforated blockages ($l_B/H = 1.5$ compared to 2.0 or higher in previous studies such as that of Moon and Lau [2]) and a narrow spacing between perforations ($S_{z2}/D_j = 2.0$). The average heat transfer correlates with that seen by Moon and Lau [2], Ahn

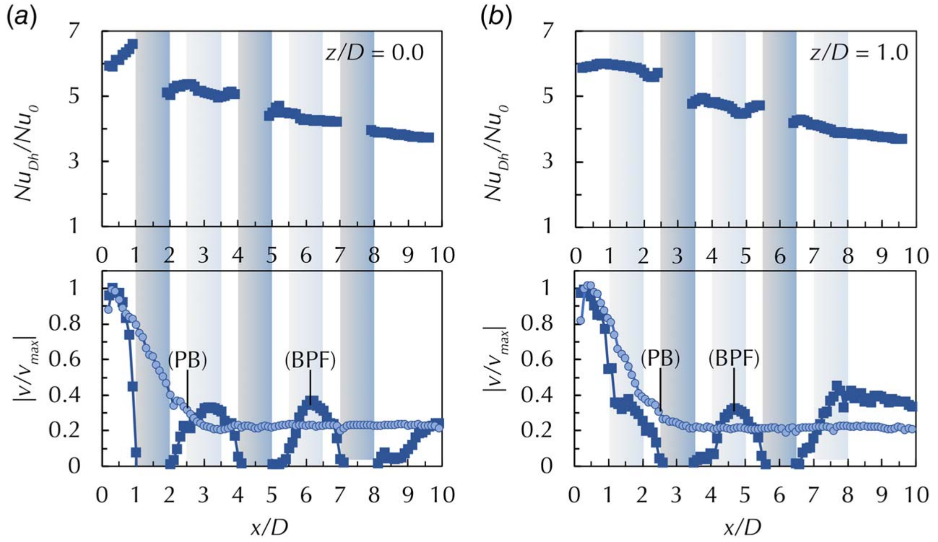

Fig. 7 One-to-one response of local Nusselt number and mid-height velocity field, and comparisons where D_j is the blockage diameter and D is the pin-fin diameter for $D/D_j = 2.0$ fixed in the present study: (*a*) extracted along x/D_j at $z/D = 0.0$ and (*b*) Extracted along x/D_j at $z/D = 1.0$

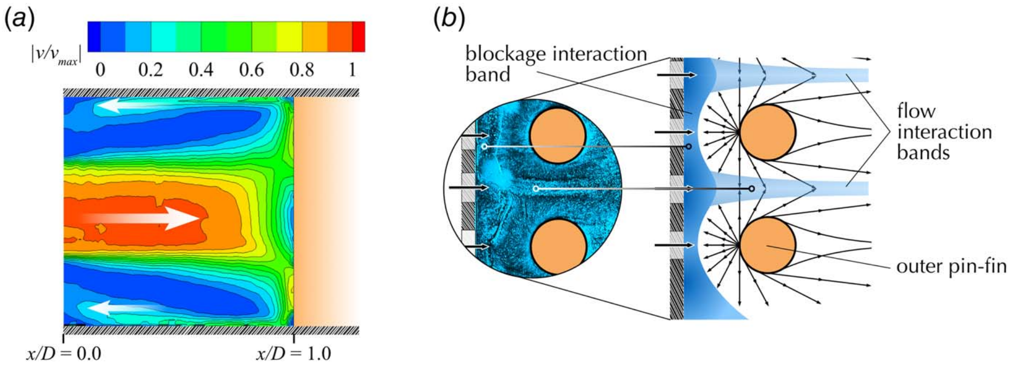

Fig. 8 Flow field at first row of pin-fins: (*a*) Velocity contour in the symmetric (*x*-*y*) plane by PIV for a pin-fin subjected to jet flow at $\mathrm{Re}_D = 35{,}000$ for a jet exit-to-pin-fin spacing of *x*/*D* = 1.0 and (*b*) oil–dye end-wall flow visualization image and corresponding flow schematic at $\mathrm{Re}_D = 26{,}000$

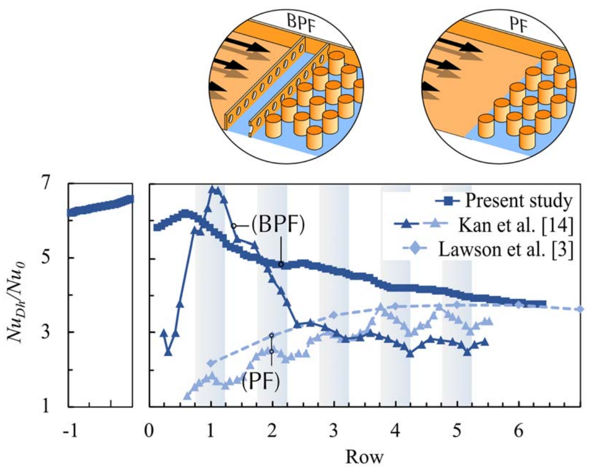

Fig. 9 End-wall heat transfer averaged in the transverse direction (the *z*-axis i.e., the channel width) for the BPF and PF configurations at $\mathrm{Re}_D = 26{,}000$

et al. [26], and Park et al. [10] for a conventional perforated blockage (PB) configuration (i.e., without downstream pin-fins).

Referring to end-wall heat transfer patterns altered by the pin-fins, the heat transfer averaged in the transverse direction (along the *z*-axis) is compared to a conventional pin-fin (PF) configuration. Note that the reference cases of Lawson et al. [3] and Kan et al. [13] used different streamwise spacings ($S_x/D = 1.73$ and $S_x/D = 2.0$, respectively), which may account for some differences. Four notable observations based on Fig. 9 are (1) the variation in end-wall heat transfer contours, (2) the difference in the end-wall heat transfer distribution between PF and BPF configurations, (3) the apparent convergence of end-wall heat transfer of the BPF and PF configurations, and (4) the large difference of end-wall heat transfer around the first pin-fin row between the present study and that by Kan et al. [13].

Around the first row of pin-fins in the BPF configuration, contour bands in the end-wall heat transfer are clearly noted. The end-wall heat transfer is, however, low, and asymmetrical surrounding the outer pin-fins (in the first row), nearest the channel walls. For the inner pin-fins, the outward radiating end-wall flow from the pin-fin (illustrated in Fig. 2(*b*)) interacts with that from neighboring pin-fins resulting in the end-wall flow field as shown in Fig. 8(*b*) where a distinct band of deposited dye between the pin-fins brought on by the interaction of end-wall flows from each pin-fin is visible. For the outer pin-fins in the first row, however, there are no neighboring pin-fins on the outer side. On their inner side, towards the channel center, the end-wall flow interacts with that from the neighboring pin-fins. However, no such interaction exists on the outer side of these pin-fins. The "flow interaction bands" between the pin-fins result in a higher heat transfer compared to the cases of no end-wall flow interaction (Fig. 6(*b*)). Note that the asymmetry in heat transfer is not due to any skewing of the jets after exiting the second blockage or any misalignment of the blockage jets. It can be considered an inherent feature of such a cooling configuration.

The end-wall heat transfer between the blockage and the first pin-fin row is significantly higher for the present study than that by Kan et al. [13] or a conventional pin-fin array (Fig. 9). This higher heat transfer is due to the end-wall flow from the pin-fin interacting with the upstream blockage. This forms a "blockage interaction band" of flow shown in Fig. 8(*b*). A poor alignment between the blockage perforations and pin-fins would result in a weaker or no blockage interaction band and hence a lower end-wall heat transfer in the region. This further emphasizes the perforations aligned with the pin-fins.

The BPF configuration resulted in the end-wall heat transfer that is consistently higher than that of a PF configuration. The area-averaged end-wall heat transfer is $\overline{\mathrm{Nu}_{Dh}}/\mathrm{Nu}_0 = 4.65$ compared to $\overline{\mathrm{Nu}_{Dh}}/\mathrm{Nu}_0 = 2.72$ for the PF configuration [3]. The higher heat transfer is attributed to the end-wall flow features unique to the BPF configuration but also the alignment between perforations and pin-fins. An argument against this might be that the space occupied by the perforated blockages could arguably limit the number of pin-fin rows that could be implemented downstream (i.e., the more perforated blockages or the larger the space between the blockages, the less space available for pin-fins). Considering a pin-fin streamwise spacing of $S_x/D = 1.5$ in the present study, the perforated blockages occupied a space of two pin-fin rows. The averaged end-wall heat transfer for the BPF configuration (from both between the blockages and around the pin-fin array) is $\overline{\mathrm{Nu}_{Dh}}/\mathrm{Nu}_0 = 5.05$. For a PF configuration of seven rows (accounting for the extra two pin-fin rows taken by the perforated blockages), the averaged end-wall heat transfer is $\overline{\mathrm{Nu}_{Dh}}/\mathrm{Nu}_0 = 3.3$ [3]. There is then a clear increase in the end-wall heat transfer offered by the inclusion of perforated blockages.

The heat transfer at the end-wall, however, only represents a portion of the heat transfer for the overall BPF configuration. The flow in the mid-height plane and the end-walls is acting on both the perforated blockages and the pin-fins directly and as such the heat transfer on these elements needs to be considered.

3.2 Heat Transfer on Perforated Blockage Surfaces.

The heat transfer on the perforated blockage surfaces is shown in Fig. 10. For both first and second perforated blockages (Figs. 10(*a*) and 10(*b*)), a clear variation across the mid-height line ($y/D = 0.5$) is observed with the upper half of the blockages ($y/D > 0.5$) having higher heat transfer. This is not due to an asymmetry in

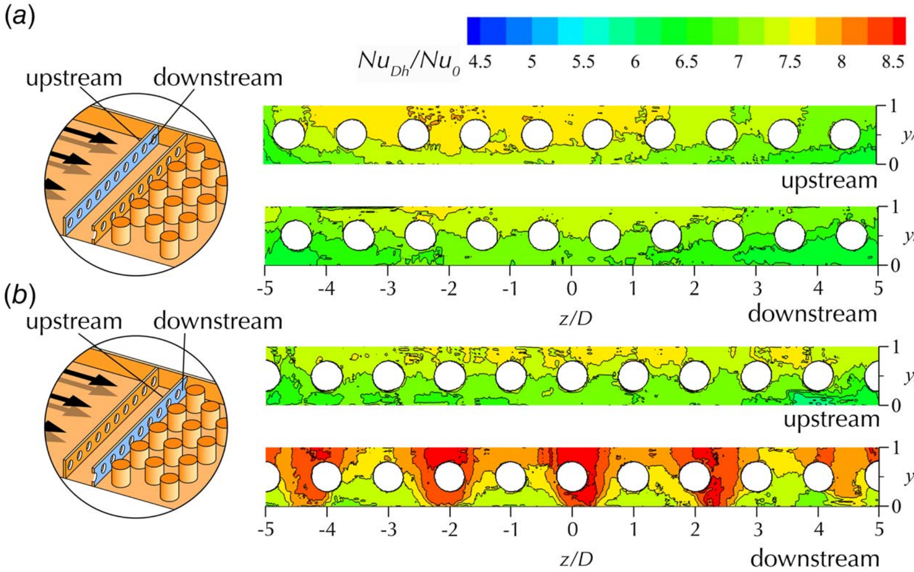

Fig. 10 Heat transfer contours measured using TLC on the surface of the perforated blockages of a blockage pin-fin configuration at $\mathrm{Re}_D = 26{,}000$: (*a*) the first blockage and (*b*) the second blockage

the flow fields across the bottom and top half of the channel. Instead, only one end-wall surface is heated, and therefore, the upper half of the perforated blockage is further from the heat source. The heat transfer across the span of the blockage (in the *z*-axis), the heat transfer is largely symmetrical about $z/D = 0.0$ for the second blockage. Higher heat transfer towards the center ($z/D = 0.0$) correlates to the end-wall heat transfer (Fig. 6(*b*)). There is a slight asymmetry on the first blockage, however. The difference is approximately $\Delta\mathrm{Nu}_{Dh}/\mathrm{Nu}_0 = 0.5$. In a review of the prior studies of perforated blockages (such as that by Moon and Lau [2] and Shin and Kwak [9], there can be seen asymmetric end-wall heat transfer contours. There is likewise a very slight asymmetry in the end-wall heat transfer between blockages and between the second blockage and first row of pin-fins (Fig. 6(*b*)). Despite the flow field in the mid-height plane appearing largely symmetrical (Fig. 6(*a*)), the resulting heat transfer appears to exhibit slightly asymmetric contours.

On the second perforated blockage (Fig. 10(*b*)), distinct vertical bands of high heat transfer on the downstream surface are formed. These vertical bands correlate with the position of the first row of pin-fins and the upstream flowing end-wall flows from these pin-fins (Fig. 8(*b*)). The flow interaction with the blockage surface results in a localized region of higher heat transfer. Less heat transfer occurs at the outer pin-fins ($z/D = \pm 4.0$).

The vertical bands are not evident on the upstream surface of the perforated blockage, despite the relatively thin blockage ($t/H = 0.25$). The upstream surface, however, is exposed to a more distributed cooling flow of ten blockage jets impinging on its surface. On the downstream surface, the cooling flow is coming from the five pin-fins in the first row with a spacing twice that of blockage jets. Despite the distinct variations in the heat transfer contours, the average heat transfer on the downstream surface of the second blockage is only $\Delta\mathrm{Nu}_{Dh}/\mathrm{Nu}_0 = 0.86$ higher than that of the upstream surface. On the first blockage, the difference between the upstream and downstream surface is smaller at $\Delta\mathrm{Nu}_{Dh}/\mathrm{Nu}_0 = 0.39$. On the second blockage, however, the downstream surface has a higher heat transfer than the upstream surface while the upstream surface has a higher heat transfer than the downstream surface. The second blockage has an average heat transfer only $\Delta\overline{\mathrm{Nu}_{Dh}}/\mathrm{Nu}_0 = 0.47$ higher than that of the first blockage.

To the best of the authors' knowledge, the heat transfer on the surface of a perforated blockage, used for cooling applications has not been presented previously. It was commented by Lau (2008) that the heat transfer on the blockages would not be negligible. Based on the present measurement data, the average heat transfer for the two perforated blockages is $\overline{\mathrm{Nu}_{Dh}}/\mathrm{Nu}_0 = 7.11$. The blockages make up 21% of the overall cooling surfaces in the configuration. Their contribution to the overall heat transfer is therefore significant, $\overline{\mathrm{Nu}_{Dh}}/\mathrm{Nu}_0 = 1.50$. Even a single perforated blockage, as used in the setup by Kan et al. [13] and Kim et al. [14], could be expected to contribute notably to the overall heat transfer performance.

3.3 Pin-Fin Heat Transfer.

The heat transfer on the pin-fins is shown in Fig. 11. The surfaces of pin-fins were painted by TLC. Converted temperature values were taken at the leading-edge, trailing-edge, and upper surface of each pin-fin. The heat transfer of these surfaces varied by less than $\Delta\mathrm{Nu}_{Dh}/\mathrm{Nu}_0 < 0.2$, indicating a negligible difference in heat transfer along the pin-fin surface. The heat transfer of the pin-fin surfaces in each row is averaged. The measurements by Chyu [27] used the naphthalene sublimation mass transfer analogy while Kan et al. [13] used the direct heat transfer measurements using TLC. The pin-fin heat transfer for the blockage pin-fin configuration was not included by Kan et al. [13] as only the central pin-fins were measured. The pin-fins in each row in that setup were not necessarily subject to the same flow conditions based on inconsistent heat transfer around the

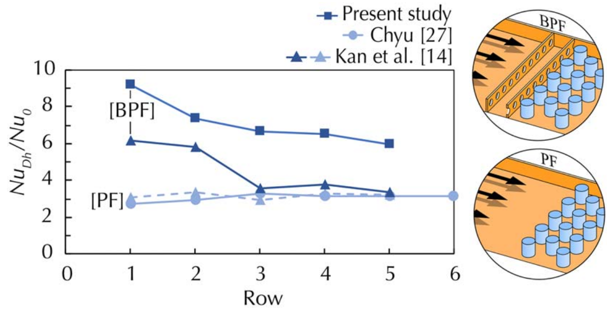

Fig. 11 Spanwise-averaged pin-fin heat transfer for a blockage pin-fin (BPF) and conventional pin-fin (PF) configurations measured using TLC at $\mathrm{Re}_D = 26{,}000$

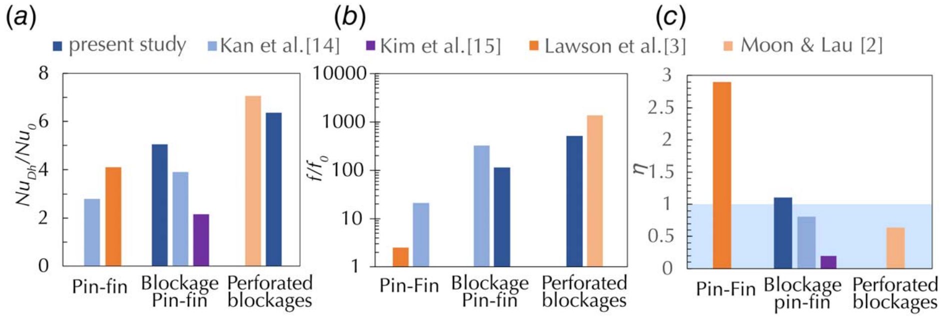

Fig. 12 Comparisons of cooling performance with different configurations: (*a*) heat transfer, (*b*) the friction factor, and (*c*) the thermal performance (η) with different cooling configurations

base of the pin-fins. Therefore, the pin-fin heat transfer values by Kan et al. [13] did not accurately represent the average heat transfer for a given row or the entire array of the blockage pin-fin configuration.

In our study, the pin-fin heat transfer for the BPF configuration is consistently higher than that of a conventional PF configuration (Fig. 11). The pin-fin heat transfer, however, decreases monotonically along the pin-fin array, similar to the end-wall heat transfer, while it remains relatively constant for a conventional pin-fin array. It is likely that the pin-fins for the BPF configuration exhibit such high heat transfer, compared to a conventional PF array due to the concentration of the cooling flow in the mid-height plane. The decrease downstream then occurs due to the diffusion of the blockage jets in the y-direction, towards the end-wall surfaces.

The average heat transfer for the pin-fins across the full array is $\overline{\mathrm{Nu}_{Dh}}/\mathrm{Nu}_0 = 6.58$ for the BPF configuration. This is more than double that of the conventional PF array. Further, the pin-fins had heat transfer that is 53% higher than the end-wall around the pin-fins (excluding the end-wall space between the perforated blockages). This difference is higher than the 35% noted by VanFossen [4] and Goldstein et al. [5] for a full pin-fin array. This is attributed to the distinctly different flow features as noted in Fig. 6, notably the concentration of the flow as aligned blockage jets in the mid-height plane. Overall, the PF array makes up 34.7% of the cooling surfaces in the present study. It, therefore, contributes $\overline{\mathrm{Nu}_{Dh}}/\mathrm{Nu}_{0_{pin-fin}} = 2.28$ to the overall heat transfer, 10.5% more than the end-wall surfaces $(\overline{\mathrm{Nu}_{Dh}}/\mathrm{Nu}_{0_{endwall}}) = 2.0$.

3.4 Thermal Performance and Summary.

The combination of perforated blockages and a pin-fin array results in consistently higher heat transfer compared to a conventional PF array. This is in all three primary regions: the end-wall $(\overline{\mathrm{Nu}_{Dh}}/\mathrm{Nu}_{0\,end\text{–}wall} = 2.18)$, perforated blockages $(\overline{\mathrm{Nu}_{Dh}}/\mathrm{Nu}_{0_{blockages}} = 1.50)$ and pin-fins $(\overline{\mathrm{Nu}_{Dh}}/\mathrm{Nu}_{0_{pin-fins}} = 2.28)$. Combined the heat transfer for the BPF configuration is $\overline{\mathrm{Nu}_{Dh}}/\mathrm{Nu}_0 = 5.96$. Further, due to the considered alignment of the perforations with the pin-fins, a greater heat transfer is attained, compared to previous ones (Fig. 12(*a*)).

There is, however, a large increase in the pressure drop through the test channel due primarily to the perforated blockages. Just across the perforated blockages, the friction factor ratio is $f/f_0 = 773.96$. Across the full BPF configuration, this decreases to $f/f_0 = 165.6$ due to the minimal pressure drop from the PF array and increased streamwise distance. These values are shown in Fig. 12(*b*) in comparison to other configurations.

The thermal performance of the BPF configuration at the Reynolds number of $\mathrm{Re}_D = 26{,}000$ is therefore $\eta = 1.1$. In contradiction to previous studies, this implies a performance greater than that of a smooth channel. This is due to two primary differences from the previous studies. First, the perforations (and therefore the blockage jets) are aligned with the pin-fins. With this change and considering only the end-wall heat transfer around the PF array alone, the thermal performance is $\eta = 0.90$. While below unity, this thermal performance is still higher than that of other BPF configurations obtained by Kan et al. [13] or Kim et al. [14]. Secondly, the consideration of the combined heat transfer on the blockage, pin-fin, and end-wall surfaces meant a more complete measure of the heat transfer taking place.

Further, the performance at different Reynolds numbers has not been considered. An increase in Reynolds numbers is noted in prior literature to result in a consistently lower thermal performance. This applies to conventional PF configurations [3], PB configurations [2], and BPF configurations [13]. The current Reynolds number $(\mathrm{Re}_{Dh} = 10{,}000)$ represents the lower end applicable to turbine blade cooling flows [28]. Tests at higher Reynolds numbers would result in thermal performances below 1.1. The thermal performance of a PF configuration is significantly higher than the current BPF configuration as per Fig. 12(*c*). There is therefore no merit in considering other Reynolds numbers using the current configuration of two perforated blockage plates and five rows of pin-fins.

Unlike a PF configuration, however, the end-wall and pin-fin heat transfer of a BPF configuration decreases along the pin-fin array (Figs. 6(*b*), 7, and 11). The averaged heat transfer for a BPF configuration would be expected to be higher if there are fewer pin-fin rows while the opposite would occur for a conventional PF array. On the other hand, fewer pin-fin rows would not significantly alter the relative pumping power given the small pressure drop through a PF array. The thermal performance of the BPF configuration would therefore increase with fewer pin-fins rows while the PF configuration would decrease for a given pumping power. There may then exist a design condition involving limited space, such as the turbine airfoil trailing-edge where a BPF configuration would produce a superior cooling performance to a conventional PF array. Additionally, the consideration of slots instead of circular perforations in the blockage plates may result in a lower pressure drop across the cooling configuration. There would however be less coolant focused on the pin-fins in the mid-height plane. These considerations are considered beyond the scope of this study. It has been shown that a blockage pin-fin configuration can achieve a thermal performance above unity and there may even be merit for its application. It is nevertheless evident that in its current form of two perforated blockages and five rows of pin-fins, the setup has a thermal performance well below that of a conventional PF array.

4 Conclusions

We revisited the thermal performance of a blockage pin-fin configuration applicable to the cooling of a gas turbine blade inside the trailing-edge. Using a series of flow field and thermal mappings by particle image velocimetry and thermochromic liquid crystal technique, respectively at $\mathrm{Re}_D = 26{,}000$, the thermal performance as a product of convective heat transfer and pressure drop was characterized and compared with other conventional cooling configurations. The present setup used two sequentially staggered perforated blockages and five rows of staggered pin-fins. The perforations of the second blockage were aligned so that the blockage jets directly impinge on the downstream pin-fins. The heat transfer from all surfaces on which the cooling flow acts, pin-fins, perforated blockages, and end-walls, was considered. The conclusions of this study are as follows:

1. A thermal performance above unity (e.g., $\eta = 1.1$) for a blockage pin-fin configuration can be achieved.
2. Due to the cooling flow being initially constrained to the mid-height plane as blockage jets, the pin-fins had heat transfer 53% higher than the end-wall heat transfer.
3. The heat transfer on the surfaces of the perforated blockages is not insignificant and contributed to 20% of the entire heat transfer for a blockage pin-fin configuration.
4. The heat transfer on the pin-fins and local end-wall decreases along the pin-fin array. The thermal performance of the blockage pin-fin configuration thus benefits from having fewer pin-fin rows.

Conflict of Interest

There are no conflicts of interest.

Data Availability Statement

The datasets generated and supporting the findings of this article are obtainable from the corresponding author upon reasonable request.

Nomenclature

h = heat transfer coefficient, $\mathrm{Wm^{-2}K^{-1}}$
f = friction factor
p = static pressure, Pa
t = thickness of perforated blockage plate, m
v = flow velocity, m/s
x = an axis coinciding with the streamwise direction of the flow and nominal jet axis
y = an axis coinciding with the axis of the pin-fins or height of the channel
z = an axis coinciding with the spanwise direction of the flow or width of the channel
A = heater surface area, $\mathrm{m^2}$
D = pin-fin diameter, m
H = test channel height, m
Q = heat input, W
T = temperature, K
W = test channel width, m
$\dot{m}$ = mass flowrate, kg/s
q'' = heat flux, $\mathrm{Wm^{-2}}$
f_0 = friction factor for smooth channel
k_f = thermal conductivity, $\mathrm{Wm^{-1}K^{-1}}$
l_B = spacing between perforated blockage plates, m
C_p = specific heat, $\mathrm{Jkg^{-1}K}$
D_j = jet diameter, m
D_h = hydraulic diameter, m
S_x = spacing between components, m
Nu = Nusselt number
Nu_0 = empty channel Nusselt number
Pr = Prandtl number
Re = Reynolds number
S_{z1}, S_{z2} = spanwise spacing between pin-fin and perforation centers, m

Greek Symbols

α = camera inclination angle, degrees
μ = dynamic viscosity, N s/$\mathrm{m^2}$
η = thermal performance
ρ = density, $\mathrm{kg/m^3}$

References

[1] Mitsubishi Power, 2023, "Mitsubishi Power' Gas Turbines Incorporate a Number of Critical Leading-Edge Technologies," Mitsubishi Power, https://power.mhi.com/products/gasturbines/?_ga=2.251965838.609179844.1682403422-443997724.1682403422, Accessed April 25, 2023.

[2] Moon, S. W., and Lau, S. C., 2003, "Heat Transfer Between Blockages With Holes in a Rectangular Channel," J. Heat Transfer, **125**(4), pp. 587–594.

[3] Lawson, S. A., Thrift, A. A., Thole, K. A., and Kohli, A., 2011, "Heat Transfer From Multiple Row Arrays of Low Aspect Ratio Pin Fins," Int. J. Heat Mass Transfer, **54**(17–18), pp. 4099–4109.

[4] VanFossen, G. J., 1982, "Heat-Transfer Coefficients for Staggered Arrays of Short Pin Fins," J. Eng. Power, **104**(2), pp. 268–274.

[5] Goldstein, R. J., and Chen, S. B., 1998, "Flow and Mass Transfer Performance in Short Pin-Fin Channels With Different Fin Shapes," Int. J. Rotating Mach., **4**(2), pp. 113–128.

[6] Baker, C. J., 1980, "The Turbulent Horseshoe Vortex," J. Wind Eng. Ind. Aerodyn., **6**(1–2), pp. 9–23.

[7] Schekman, S., Atkins, M. D., and Kim, T., 2019, "Local End-Wall Heat Transfer Enhancement by Jet Impingement on a Short Pin-Fin," Int. J. Heat Mass Transfer, **128**, pp. 1033–1047.

[8] Lau, S. C., Cervantes, J., Han, J. C., and Rudolph, R. J., 2008, "Internal Cooling Near Trailing Edge of a Gas Turbine Airfoil With Cooling Airflow Through Blockages With Holes," ASME J. Turbomach., **130**(3), p. 031004.

[9] Shin, S., and Kwak, J. S., 2008, "Effect of Hole Shape on the Heat Transfer in a Rectangular Duct With Perforated Blockage Walls," J. Mech. Sci. Technol., **22**(10), pp. 1945–1951.

[10] Park, J. S., Jo, Y. H., and Kwak, J. S., 2016, "Heat Transfer in a Rectangular Duct With Perforated Blockages and Dimpled Side Walls," Int. J. Heat Mass Transfer, **97**, pp. 224–231.

[11] Metzger, D. E., Fan, C. S., and Haley, S. W., 1984, "Effects of Pin Shape and Array Orientation on Heat Transfer and Pressure Loss in Pin Fin Arrays," ASME J. Eng. Gas Turbines Power, **106**(1), pp. 252–257.

[12] Lyall, M. E., Thrift, A. A., Thole, K. A., and Kohli, A., 2011, "Heat Transfer From Low Aspect Ratio Pin Fins," ASME J. Turbomach., **133**(1), p. 011001.

[13] Kan, R., Ren, J., and Jiang, H., 2014, "Combined Effects of Perforated Blockages and Pin Fins in a Trailing Edge Internal Cooling Duct," Proceedings of the ASME Turbo Expo 2014: Turbine Technical Conference and Exposition., Düsseldorf, Germany, June 16–20.

[14] Kim, Y., Choi, S. M., Park, H. S., Kim, S. W., Jung, E. Y., Park, J. S., and Cho, H. H., 2019, "Heat Transfer Characteristics of the Rib Angle in the Pin-Fin Cooling Combined With Perforated Blockage," Trans. Korean Soc. Mech. Eng. B, **43**(7), pp. 453–461.

[15] Ward-Smith, A. J., 1971, *Pressure Losses in Ducted Flow*, Butterworth, Oxford.

[16] Liu, Y. Y., Schekman, S. W., Bhaiyat, T. I., Lu, T. J., and Kim, T., 2022, "Impingement Cooling of an Isoflux Flat Plate by Blockage Jet," Appl. Therm. Eng., **209**(118239), pp. 1–12.

[17] McNaughton, K. J., and Sinclair, C. G., 1966, "Submerged Jets in Short Cylindrical Flow Vessels," J. Fluid Mech., **25**(2), pp. 367–375.

[18] Atkins, M. D., and Kim, T., 2015, "Isotropic-Planar Illumination for PIV Experiments," *Exp. Fluids*, 56(3), p. 63.

[19] Kim, T., Lu, T. J., and Song, S. J., 2016, *Application of Thermo-Fluidic Measurement Techniques: An Introduction*, Butterworth-Heinemann, Oxford.

[20] Kays, W. M., and Crawford, M. E., 1993, *Convective Heat and Mass Transfer*, McGraw-Hill, New York.

[21] Kakac, S., Shah, R. K., and Aung, W., 1987, *Handbook of Single-Phase Convective Heat Transfer*, John Wiley & Sons Inc., Hoboken, NJ.

[22] Coleman, H. W., and Steele, W. G., 2018, *Experimentation, Validation, and Uncertainty Analysis for Engineers*, John Wiley & Sons, New Jersey.

[23] Westerweel, J., 1997, "Fundamentals of Digital Particle Image Velocimetry," Meas. Sci. Technol., **8**(12), pp. 1379–1392.

[24] Westerweel, J., 2000, "Theoretical Analysis of the Measurement Precision in Particle Image Velocimetry," Exp. Fluids, **29**(7), pp. S003–S012.

[25] Westerweel, J., 2008, "On Velocity Gradients in PIV Interrogation," Exp. Fluids, **44**(5), pp. 831–842.

[26] Ahn, H. S., Lee, S. W., Lau, S. C., and Banerjee, D., 2007, "Mass (Heat) Transfer Downstream of Blockages With Round and Elongated Holes in a Rectangular Channel," J. Heat Transfer, **129**(12), pp. 1676–1685.

[27] Chyu, M. K., 1990, "Heat Transfer and Pressure Drop for Short Pin-Fin Arrays With Pin-Endwall Fillet," J. Heat Transfer, **112**(4), pp. 926–932.

[28] Han, J. C., 2013, "Fundamental Gas Turbine Heat Transfer," ASME J. Therm. Sci. Eng. Appl., **5**(2), p. 021007.